

Application of the steady laminar flamelet model for humidified non-premixed swirl flames: effects of water vapor addition on nox emissions

A. Guessab*, M. Bounouar, M. Mokhtari

Mechanical Manufacturing Technology Research Laboratory, National Polytechnic School of Oran, 1523 EL M'Naouar Es-Senia, Oran, Algeria
email: ahmed.guessab@enp-oran.dz

Abstract

This study examines turbulent diffusion flames in a combustion chamber, academically known as the Burner Engineering Research Laboratory. We used the Steady Laminar Flamelet combustion model with a detailed oxidation mechanism for natural gases from GRI-3.0. The simulation results were validated against experimental data for velocity fields, temperature, and the mass fraction of chemical species, and strong consensus was observed. Through this simulation, we focused on the effect of adding and injecting water vapor into the combustion chamber as an emission control strategy. Humidifying the fuel significantly reduces nitric oxide (NO) formation by decreasing the maximum flame temperature and residence time, while diluting the air through the addition of water vapor amplifies NO concentrations. The results demonstrate the advantage of combining detailed chemistry with elemental flame modeling for emission control prediction. This technique is a promising strategy for cleaner combustion, especially in industrial settings. Ultimately, this numerical study directly contributes to the potential reduction of pollutant emissions, particularly NO_x and CO, which is our goal in the fight against air pollution and climate change.

Keywords: water vapor, GRI-3.0, SLFM, NO_x emissions.

PACS numbers: 82.20.Wt, 47.70.Pq

<i>Received:</i>	<i>Revised:</i>	<i>Accepted:</i>	<i>Published:</i>
22 September 2025	26 December 2025	18 February 2026	31 May 2026

1. Introduction

Combustion is a method of energy conversion, and turbulence is fundamental to increasing efficiency and reducing pollutant emissions. In recent years, several models that address the coupling between turbulence and the kinetic chemistry of oxidation have been developed and integrated into numerical codes for computational fluid simulation.

The most popular models are the eddy dissipation model (EDM), the eddy dissipation concept (EDC), chemical equilibrium (CE), flamelet models, the flamelet-generated manifold (FGM), and the transported probability density function (T-PDF) approach [1, 2].

The flamelet model has become essential in the numerical simulation of turbulent combustion flames due to its ability to combine detailed turbulence and chemical kinetics within the flame structure. This model was initially developed in the 1970s [3] and has been successfully applied to various types of flames.

A key advantage of this model lies in its ability to provide reliable predictions of temperature and chemical composition fields without directly solving all the transport equations for the chemical species, while simultaneously reducing computational cost and preserving the influence of detailed chemical kinetics and mixture fraction gradients.

Given that the flamelet model is widely used in large eddy simulations (LES) [4–7], the same model has generally adapted well and appears effective in modeling with the Reynolds statistical averaging method [8–10].

Several studies have investigated the structure of the flame and even the formation of NO_x using this model, and some examples include [12–16]. The advantage of the SLF model compared to the EDC model is that the flamelet model does not require a high-quality mesh, which means that for more complex geometries, or where further refinement is needed in specific areas, the SLF model is better suited to these geometries and does not require additional refinement.

We chose the BERL combustion chamber configuration because it represents a real-world case that links laboratory research with industrial applications. This combustion chamber is known experimentally, or its measurement data is freely accessible. The flame developing inside this chamber serves to validate our calculation. The data from the IFRF experimental studies referenced in [17] and the numerical calculations referenced in [18-20] provide important data for validating our calculations. We can cite some studies based on the effect of using detailed chemical kinetic mechanisms on the evolution of flame temperature as well as on its speed [21–24].

All research on the phenomenon of turbulent combustion in various industrial applications aims to define and reduce all pollutant emissions, such as NO_x, generally focusing on nitrogen oxides (NO). The creation of these species is due to high temperatures. Several techniques can be applied to lower these pollutant emissions.

These techniques allow for a reduction in flame temperature and the residence time to be minimized. In practice, the technique of adding water vapor is used [25]. This technique is better and less expensive, even with low loads in the installations. It involves using a sprayer that injects the vapor either into the fuel or into the air, where it reacts with the fuel.

Table 1 provides an illustration and an idea of the techniques that can be used for NO_x reduction.

Fuel dilution with the addition of water vapor	Air dilution with addition of water vapor
<ul style="list-style-type: none"> • Water-fuel emulsion by finely mixing water with liquid fuel • Direct water injection into the combustion chamber • Hydrated fuels such as hydrated ethanol 	<ul style="list-style-type: none"> • Humidifying intake air by passing it through a humidifier • Direct injection of water vapor • Recirculating humid exhaust gases (EGR) • Utilizing natural humidity of ambient air in appropriate climates

Table 1. Methods for incorporating water vapor into the combustion process

This work is devoted to the use the SLFM to model turbulent diffusion natural gas flames in a BERL combustor and to examine the capability of this combustion model to predict the main flame characteristics, namely, temperature, velocity, and species distributions, while also investigating the effectiveness of water vapor addition as a strategy for reducing NO_x emissions.

Through these numerical simulations, the results were compared with experimental results to lend credibility to the work presented in this article, and parametric analyses were conducted by varying the water vapor mass fraction in the range of 0–25%.

2. Mathematical model

2.1. Geometrical configuration and operating conditions

Figure 1a shows the complete geometry of the BERL combustor used in this study. A concise description of the burner dimensions is provided in this study, and further details can be found in [2, 26]. The figure 1b also shows the longitudinal section (detailed view) of

the combustion chamber. The burner dimensions were based on the outer diameter of the combustion air duct ($D_o = 87$ mm). The injector was equipped with 24 radial gas holes, each with a diameter of $D_{holes} = 1.8$ mm. The fuel was supplied through the longitudinal tube. The operating conditions were as follows: Airflow quantity was 0.11832 kg/s at 312.15 K, and the fuel flow rate was 0.006 kg/s at 308.15 K. The swirled flow upstream of the burner chamber produced a swirl number of 0.56 in the air annulus. Computational domain was extended by 3 m axially and 1.0668 m radially.

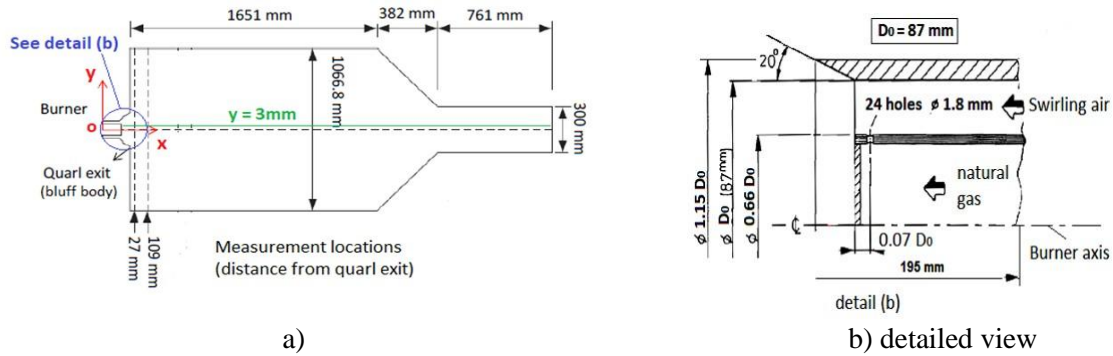


Figure 1. a) Schematic representation of the 300 kW BERL furnace, b) Enlarged view of the burner section

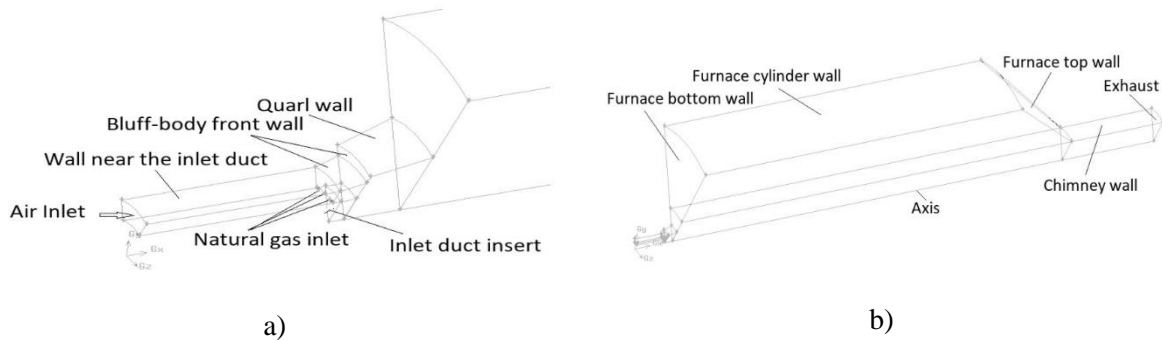


Figure 2. Nomenclature of the furnace walls used for the boundary condition

Inlet	Fuel radial velocity	157,25 (m/s)
	Fuel inlet turbulent intensity	5 %
	Fuel temperature	308,15 (K)
	Air axial velocity	Profile (Fig.3)
	Air swirl velocity	Profile (Fig.3)
	Air turbulent intensity	17%
	Air temperature	312,15 (K)
	Air turbulence length scale	0.0076 (m)
	Fuel turbulence length scale	0.0009 (m)
Furnace wall boundary conditions (Fig. 2)	Wall near inlet ducts	312 (K)
	Bluff body front wall	1173 (K)
	Inlet duct insert	1173 (K)
	Quarl wall	1273 (K)
	Lower wall of combustion chamber	1100 (K)
	The cylindrical wall of the combustion chamber	1280 (K)
	The wall at the top of the combustion chamber	1305 (K)
	Vertical canal wall	1370 (K)
Outlet type	Pressure outlet	

Table 2. Inlet and outlet boundary conditions [2]

The fuel employed contains 98.4% CH₄, 0.3% CO₂, and 1.3% N₂. The mixture of air, comprising 21% O₂ and 79% N₂ by mass, served as the oxidizer. Based on the fuel jet, the Reynolds number was approximately 320,000. The information used in the simulations is identical to the information used in the experiments in table 2. The diagram demonstrates the classification of the furnace walls of the BERL combustor. The labels for different wall sections were created based on their respective boundary conditions, thereby providing a clear reference for the numerical setup and ensuring consistency in the simulation framework (ANSYS FLUENT). The inlet and outlet conditions are shown in figure 3.

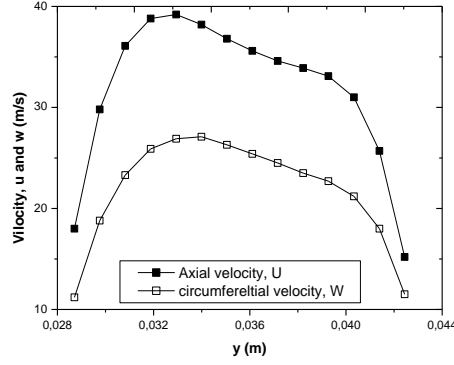


Figure 3. Inlet U and W velocity components [2]

2.2. Governing equations

The conservative equations that represent this type of flow are

$$\frac{\partial \rho}{\partial t} + \nabla \cdot (\rho u) = 0 \quad (1)$$

$$\frac{\partial (\rho u)}{\partial t} + \nabla \cdot (\rho u u) = -\nabla p + \nabla \cdot \mu_{eff} \nabla u + \nabla u^t + \rho g \quad (2)$$

$$\frac{\partial (\rho h)}{\partial t} + \nabla \cdot (\rho u h) = \nabla \cdot (\lambda_{eff} \nabla T) + S_h \quad (3)$$

where, ρ is the fluid density and u are the velocity vector. h is the specific enthalpy, T is the temperature, and λ_{eff} is the effective thermal conductivity (laminar + turbulent). The source term S_h accounts for the contribution of chemical reactions.

$$\frac{\partial (\rho Y_i)}{\partial t} + \nabla \cdot (\rho u Y_i) = -\nabla \cdot J_i + R_i \quad (4)$$

In this expression, Y_i is the mass fraction of species, J_i is the diffusion flux, and R_i is the net rate of production of consumption of species i due to chemical reactions.

This equation guarantees the conservation of mass for each chemical species involved in the combustion.

$$\frac{\partial (\rho k)}{\partial t} + \nabla \cdot (\rho u k) = \nabla \cdot \left(\left(\mu + \frac{\mu_t}{\sigma_k} \right) \cdot \nabla k \right) + G_k - \rho \varepsilon \quad (5)$$

$$\frac{\partial (\rho \varepsilon)}{\partial t} + \nabla \cdot (\rho u \varepsilon) = \nabla \cdot \left(\left(\mu + \frac{\mu_t}{\sigma_\varepsilon} \right) \cdot \nabla \varepsilon \right) + \rho C_1 S \varepsilon - C_2 \rho \frac{\varepsilon^2}{k + \sqrt{v \varepsilon}} \quad (6)$$

$$\mu_t = \rho C_\mu \frac{k^2}{\varepsilon} \quad (7)$$

Where: Gk is the production of turbulent kinetic energy owing to mean gradients and σk is the turbulent Prandtl number for k . With model-specific coefficients that vary with the local field. Here, $C\mu$ is an empirical constant that is typically set to 0.09.

Mixture fraction (f) transport equation.

$$\frac{\partial(\rho f)}{\partial t} + \nabla \cdot (\rho u f) = \nabla \cdot \left(\left(\mu + \frac{\mu_t}{\sigma_t} \right) \cdot \nabla f \right) \quad (8)$$

Mixture fraction variance (f''^2) transport equation:

$$\frac{\partial(\rho f''^2)}{\partial t} + \nabla \cdot (\rho u f''^2) = \nabla \cdot \left(\left(\mu + \frac{\mu_t}{\sigma_t} \right) \cdot \nabla f''^2 \right) - 2\rho\chi \quad (9)$$

Where: σ_f is the turbulent Schmidt number and, f''^2 is the variance of the mixture fraction fluctuations, and χ is the scalar dissipation rate.

Scalar dissipation rate (χ)

$$\chi = 2D(\nabla f \cdot \nabla f) \quad (10)$$

where D denotes the molecular diffusivity. The scalar dissipation rate characterizes the rate at which fluctuations in the mixture fraction are smoothed via molecular diffusion.

2.3. Numerical methods

The flow turbulent was designed using a Realizable $k - \varepsilon$ model with scalable wall functions so that it could be used near the wall. As for representing the radiative heat transfer, we used the model called discrete ordinates (DO) [2]. The finite volume method (FVM) is used by the Luent calculation code for the description of the differential equations of the flow and for the modeling of pressure – velocity the coupled method is used.

A second-order upwind scheme was applied for the momentum and scalar transport discretization. As for the walls of the combustion chamber, we stipulated that they must not move, meaning they must be fixed walls, and zero normal pressure gradients were applied at the boundaries. In this study, the chemical kinetics mechanism for natural gas of GRI-3.0 [28] was used.

2.4. Mesh independence study

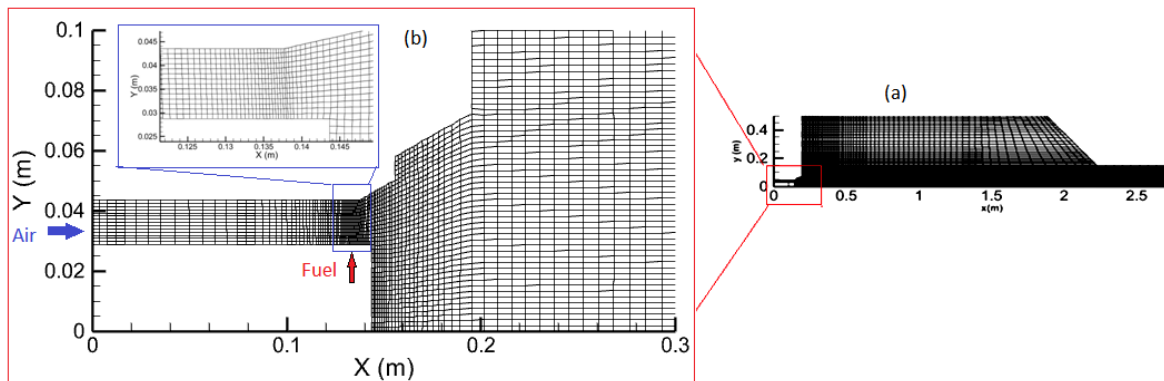


Figure 4. a) 2D-axisymmetric mesh, b) detailed view

The combustion chamber mesh was generated using GAMBIT 2.2 [29] (figure 4). The mesh density was optimized to minimize numerical diffusion and ensure the stability and

convergence of the simulation. Convergence was achieved when the residuals fell below 10^{-6} . Every computation was predicated on 2D-axisymmetric configuration.

Before launching any numerical simulation calculations, it is crucial to ensure two things: the selection of a suitable mesh and the study of its independence. In our case, we selected the GRI-3.0 reaction mechanism for natural gas oxidation, and for combustion modeling, we chose the SLF model, as justified in the introduction. For this study of independence and mesh selection, we will focus on the evolution of the three most important parameters in the simulation of turbulent combustion: the flame temperature, the axial velocity, and the oxygen species. Three different types of mesh are selected for this mesh independence test: mesh 1 with 9784 cells, mesh 2 with 12784 cells, mesh 3 with 20456 cells figures 5 and 6 illustrate the evolution of the axial profiles of flame temperature and axial velocity on the line which has a distance of $y = 3$ mm from the axis of the combustion chamber. The temperature forecasts from every mesh displayed similar patterns, with maximum values of 1893, 1913, and 1907 K for the grid 1 (9784 cells), grid 2 (12784 cells), and grid 3 (20456 cells), respectively Nevertheless, the values we obtained are in agreement and very close to the values of the experimental results we used for comparison. During the experimental measuring, the maximum temperature reached 1942.55 K, with a fluctuation of less than 2.5% between grid 1 and grid 3. The grid 1 a little underestimated the results near the injector and overestimated them downstream, while the grid 2 and grid 3 provided almost identical results across the total domain. Figures 7 and 8 illustrate the radial profiles of O_2 and temperature at $x = 27$ mm, respectively. In general, grid 2 and grid 3 produced comparable results, thus proving that the mesh is independent of its size. Due to the reduced computational cost, a grid 2 (12,784 cells) was chosen for the following analyses.

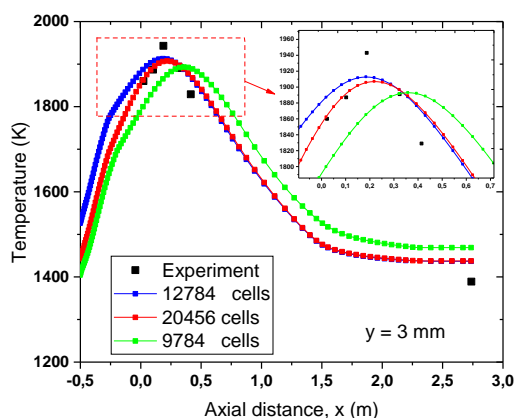


Figure 5. Radial profiles of flame temperature at position $y = 3$ mm

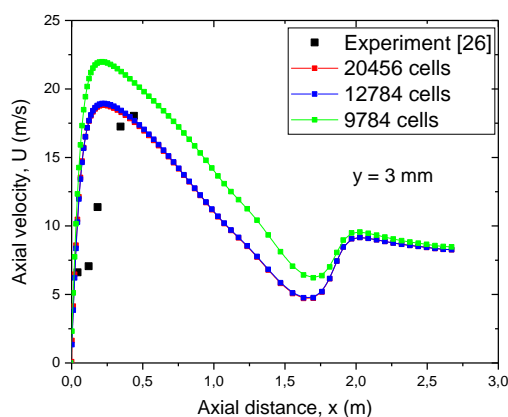


Figure 6. Radial profiles of axial velocity at position $y = 3$ mm

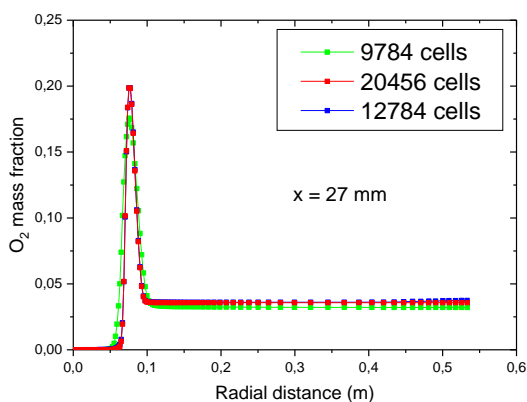


Figure 7. Radial profiles of the mass fraction at of the O_2 species at position $x = 27$ mm

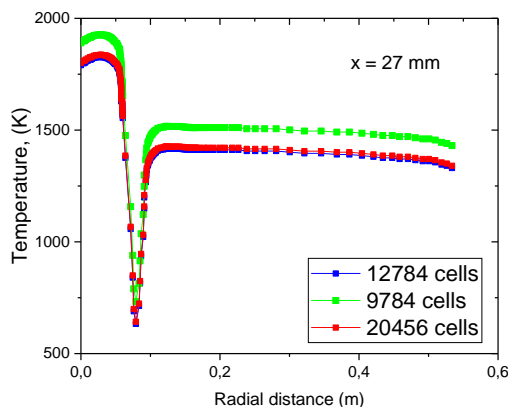


Figure 8. Radial profiles of flame temperature position $x = 27$ mm

2.5. Flamelet library for Natural gas /Air flame

Figure 9 shows how the flame temperature varies with the scalar fraction of the mixture. The graph illustrates a rapid decrease in flame temperature, from approximately 2200 K for a scalar mixture fraction ($f = 0$) to approximately 300 K for a scalar mixture fraction ($f = 1$). This variation is characterized by the temperature distribution and pattern within a flame, where maximum temperatures are typically observed near the stoichiometric mixture fractions. A maximum flame temperature of approximately 2075.51 K was observed for a stoichiometric mixture fraction equal to $f_{st} = 0.0574$. Figure 10 illustrates the radial evolution of the flamelets for the mass fractions of the chemical species CO_2 , CO , and H_2O . Overall, the estimated profiles of CO_2 , CO , and H_2O coincide well, thus validating the flamelet method.

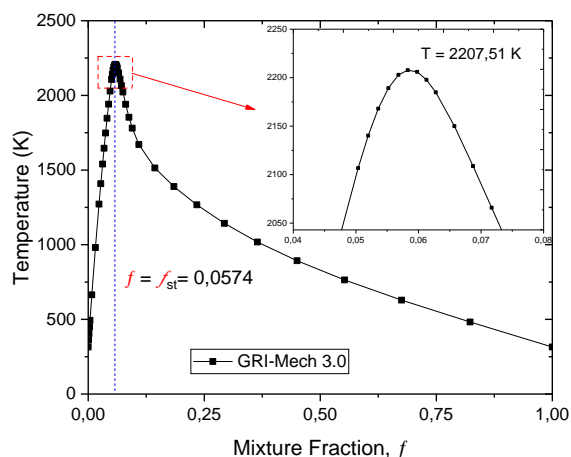


Figure 9. Flamelet temperature profiles

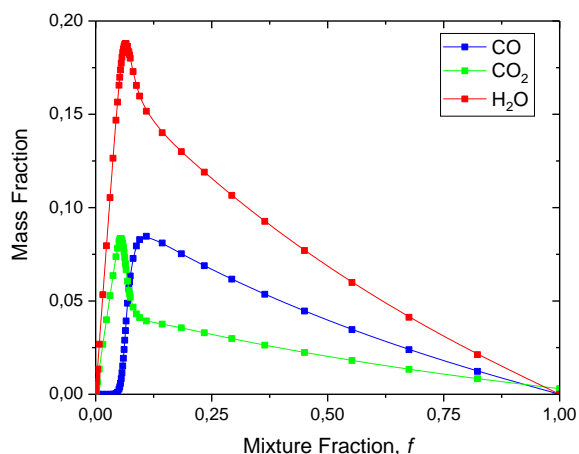


Figure 10. Flamelet profiles for mass fraction of CO_2 , CO and H_2O

3. Results

3.1. Temperature predictions

Figure 11 shows the evolution of temperatures inside the combustion chamber for two different stations taken along the chamber axis, as follows for $x = 27$ mm and $x = 109$ mm.

At both locations along the combustion chamber axis, the results obtained using the GRI-3.0 mechanism with SLF model, there is agreement between the numerical simulations we performed and the results obtained from the experiments [26, 28], particularly in capturing the maximum temperature near the flame front and the subsequent decay in the outer radial regions. The use of the EDC combustion model with the 4-step kinetic chemistry reaction mechanism studied in reference [21] gives an underestimation of the flame temperature on the combustion chamber axis or the gradient on the flame fronts, and less estimates this tendency to continue to diverge in the far region of the flame. In the region near the injector at $x = 27$ mm, the SLFM combustion model correctly reproduces the temperature behavior of the flame which gives rise to a stable zone for the flame. In the region furthest from the injector outlet at $x = 109$ mm, the continuous SLFM combustion model accurately represented the temperature distribution calculated numerically and obtained experimentally. The SLFM model, coupled with the detailed mechanism of GRI-3.0, captured the temperature peak in this region. These results prove the power of the SLFM model for the qualitative and quantitative representation of flame structure behavior. We have drawn up a table 3 which compares the maximum flame temperatures for the measurement station along the axis of the flame, that of $x = 27$ mm and that of $x = 109$ mm, with those obtained experimentally cited in reference [26], and at the same time we use another numerical study cited in reference [21] for the validation of our work. The work cited in reference [21] using EDC as a model for combustion modeling with an overall four-stage process. The EDC model's predictions were farther from the

experimental measurements than the SLFM predictions at both positions. The EDC model overestimated the temperature by 2047 K vs. 1910.73 K at 27 mm, while the present work slightly underestimated it (18878.5 K), which was within a reasonable deviation. The SLFM prediction (1973.77 K) was much more accurate for $x = 109$ mm than the EDC result (2252.53 K), which overestimated the flame temperature significantly. It has been confirmed that the utilization of GRI-Mech 3.0 in the SLFM framework enhances the predictive accuracy by capturing both near-field and far-field flame temperatures with a lesser error compared to experimental benchmarks.

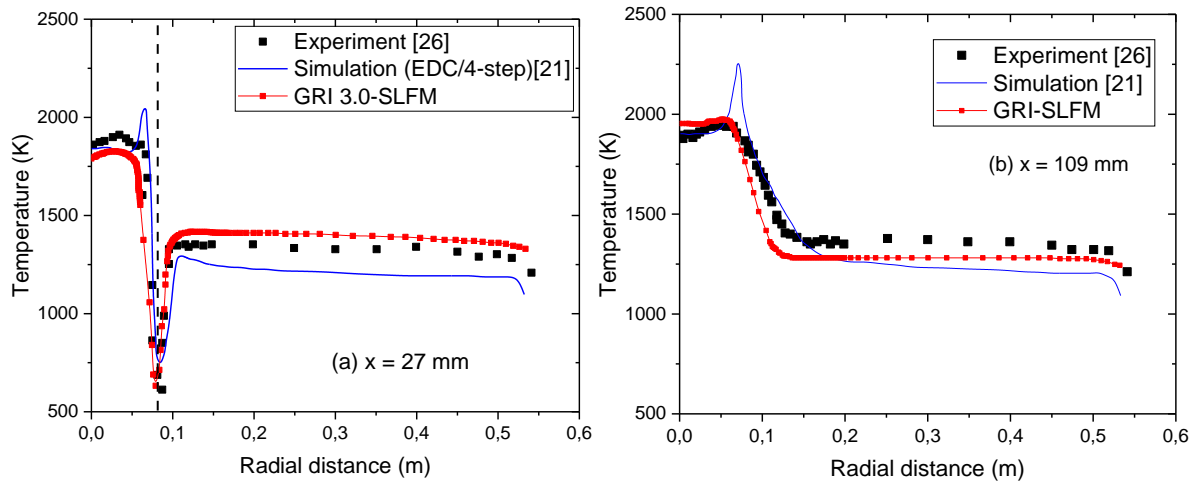


Figure 11. Temperature profiles at two locations, at $x = 27$ mm and at $x = 109$ mm

Position	Experiment [26]	Numerical study (EDC/4-step) [21]	Present Work
$x = 27$ mm	1910,73 K	2047 K	1878,5 K
$x = 109$ mm	1947.84 K	2252.35 K	1973.77 K

Table 3. Examining the maximum flame temperatures at two locations: at $x = 27$ mm and $x = 109$ mm

3.2. Velocity profiles

The axial velocity evolution at different positions along the combustion chamber axis is shown in figure 12, where it is compared with experimental results. In general, these results show better agreement between the two. For the measurement station ($x = 27$ mm), the opposing velocities defined in the internal recirculation zone were higher than those measured experimentally. Subsequently, the simulation showed a negative velocity of approximately -17 m/s on the central axis of the combustion chamber, while experimental measurements showed only -8 m/s as the velocity value at the same positions. This difference between the two values may be due to the first-order turbulence model's inability to accurately determine the anisotropy and dissipation in this region, which is dominated by strong vortex recirculations linked to highly turbulent flow.

This discrepancy can be attributed to the limited capability of the turbulence model to represent anisotropy and dissipation in the highly turbulent recirculation region. In contrast, the simulation with the GRI-Mech 3.0 mechanism produced peak values that were in closer agreement with the experimental data at both measurement stations. In general, the axial velocity field was well captured, particularly near the nozzle. The swirl velocity components are depicted in figure 13, where the results predicted through simulation are in good agreement with the experimental, up to $y = 0.1$ m, but show increasing deviations both qualitatively and quantitatively further downstream.

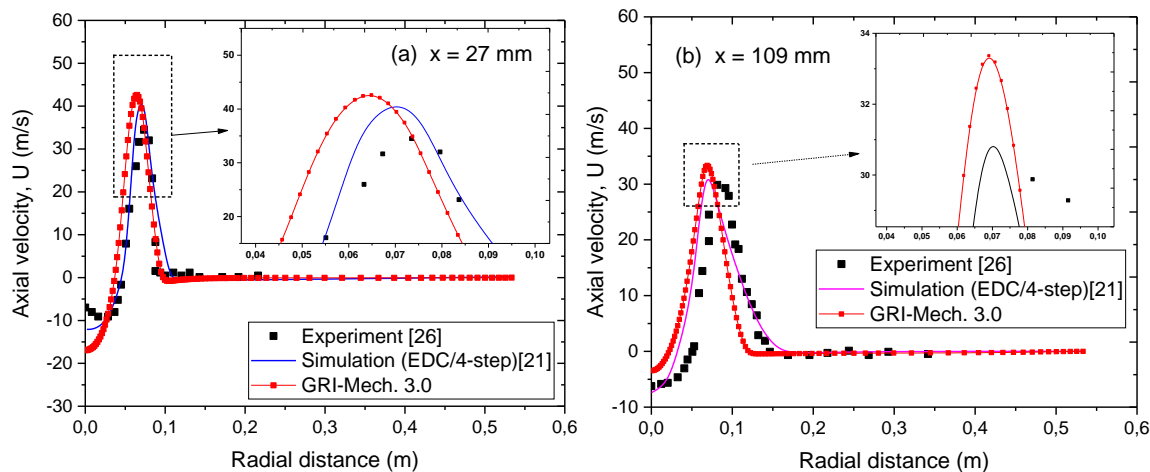


Figure 12. Radial profiles of axial velocity, U (m/s): a) $x = 27$ mm, b) $x = 109$ mm

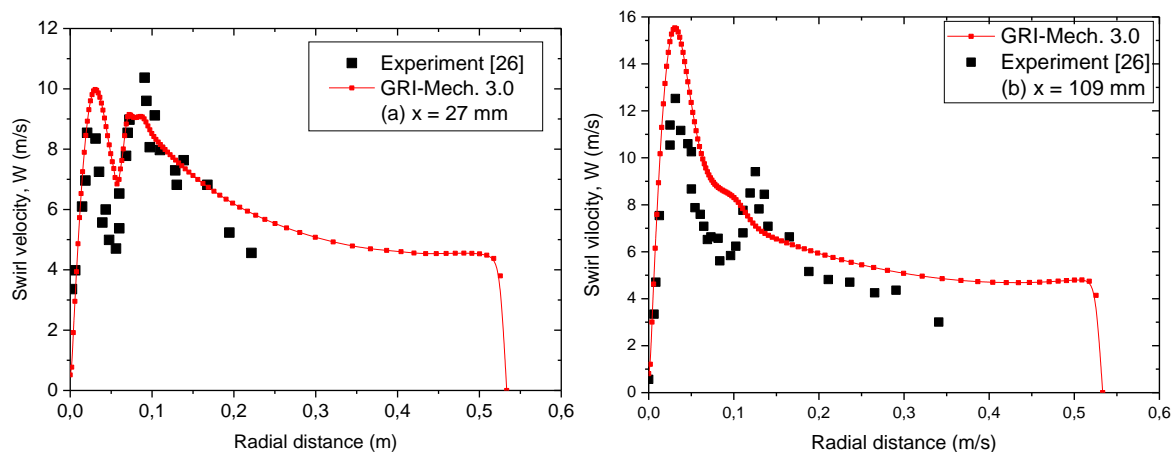


Figure 13. Radial profiles of swirl velocity W (m/s): a) $x = 27$ mm, b) $x = 109$ mm

3.3. Radial profiles of mass fractions of O_2 and CO_2

Figure 14 shows the radial distributions of the O_2 mass fraction. At $x = 27$ mm, the predictions using the GRI-Mech 3.0 mechanism reproduced a peak value of the O_2 mass fraction, which was in good concordance with the experimental data (figure 14a). At $x = 109$ mm, the detailed mechanism yielded slightly lower peak values, which improved consistency with the experimental results. Overall, the predicted profiles showed good agreement with the measurements, although oxygen burnout was under-predicted at the first station. This underestimation corresponded to a lower predicted CO_2 mole fraction at the same location. From figure 14, it can be observed that the detailed mechanism provided only marginal improvements in predicting the O_2 radial distributions at $x = 109$ and 343 mm. Figure 15 shows the CO_2 mass fraction distribution curve. The profiles obtained using the GRI-Mech 3.0 mechanism agreed reasonably well by means of the experimental data, except for a slight radial shift toward the burner. Although both models adequately predicted fuel consumption, neither captured CO_2 formation with high accuracy.

In particular, the flame model tended to overestimate both the peak values and O_2 and CO_2 mass fractions along the flame axis. This behavior is consistent with the overestimation of the differential diffusion effects incorporated in the flamelet library, which accounts for the observed discrepancies.

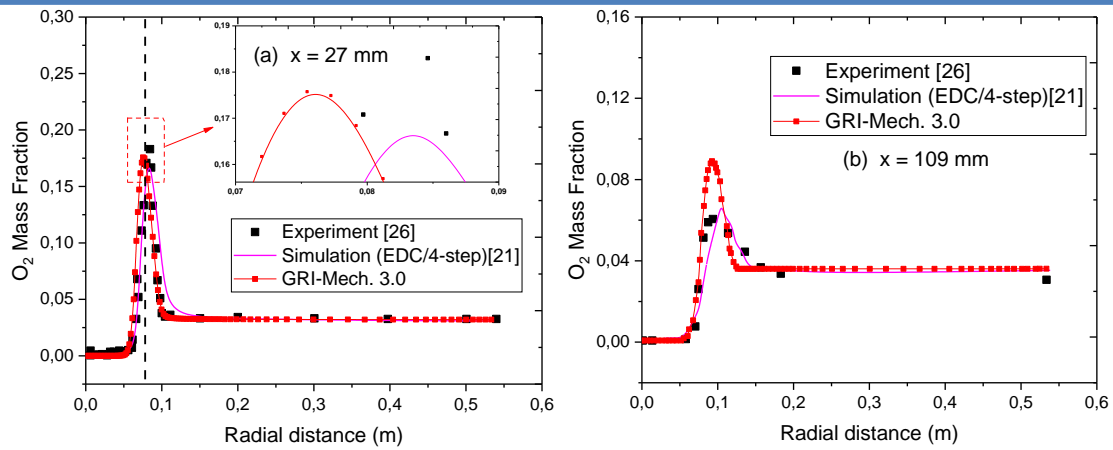


Figure 14. Radial profiles of O₂ mass fraction: (a) at x= 27 mm, (b) x = 109 mm

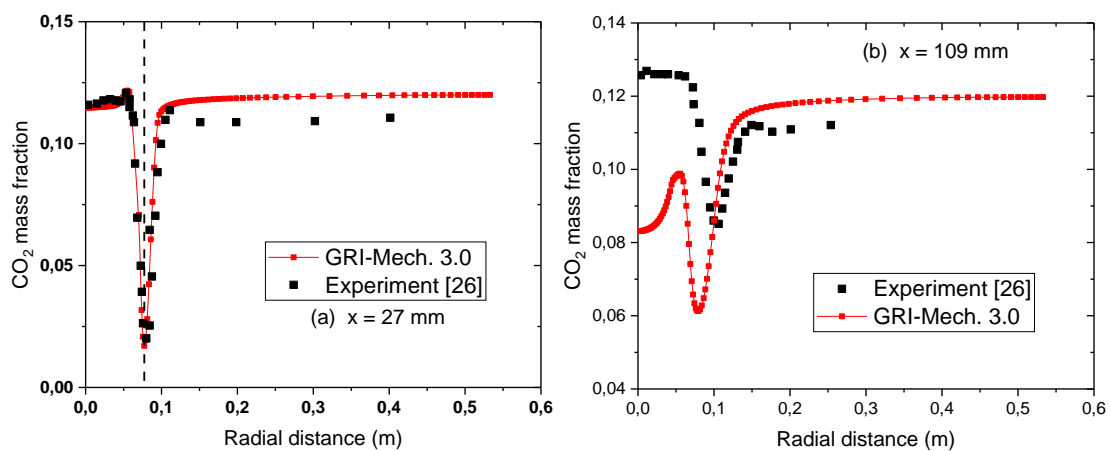


Figure 15. Radial profiles of the mass fraction of CO₂ (a) at x= 27 mm, (b) x = 109 mm.

3.4. Effect of H₂O addition to the fuel and air

This study investigated the effect of water vapor addition on the combustion characteristics, such as temperature and emissions (CO₂, CO, and NO), of a swirl-stabilized natural gas burner. All other fuel and air jet parameters were kept constant, as shown in table 2. The water vapor mass fraction was varied in increments of 5% from 0% to 25%. Data analysis indicated that when water vapor was incorporated into the fuel at a mass fraction of 25%, water contributed approximately 2% of the total mass of the mixture. Moreover, the overall mass flow rate through the burner increased with the addition of water vapor to the fuel. In the context of this study, 12 simulations were performed to evaluate the effect of adding water vapor to the combustion chamber. Generally, emissions produced by natural gas combustion are primarily composed of nitrogen oxides (NO_x), carbon monoxide (CO), carbon dioxide (CO₂), and other minor pollutants. Figure 16 shows the distribution of NO as a function of the percentage of water vapor contained in methane and in air. Ultimately, there are 12 cases to study using numerical simulation. In both graphs, we note that the amount of NO released during combustion decreases as the amount of water vapor ejected increases, either into the methane or the air. We can observe that injecting water vapor into the methane results in a lower amount of NO and a rapid decrease compared to injecting it into the air. Figure 16b illustrates the evolution of flame temperature as a function of the percentage of water vapor added to both sides (methane and air). It is clear that the temperature at the combustion chamber outlet decreases rapidly compared to the temperature at which water vapor is injected into the air; a statistical comparison can be made for each case.

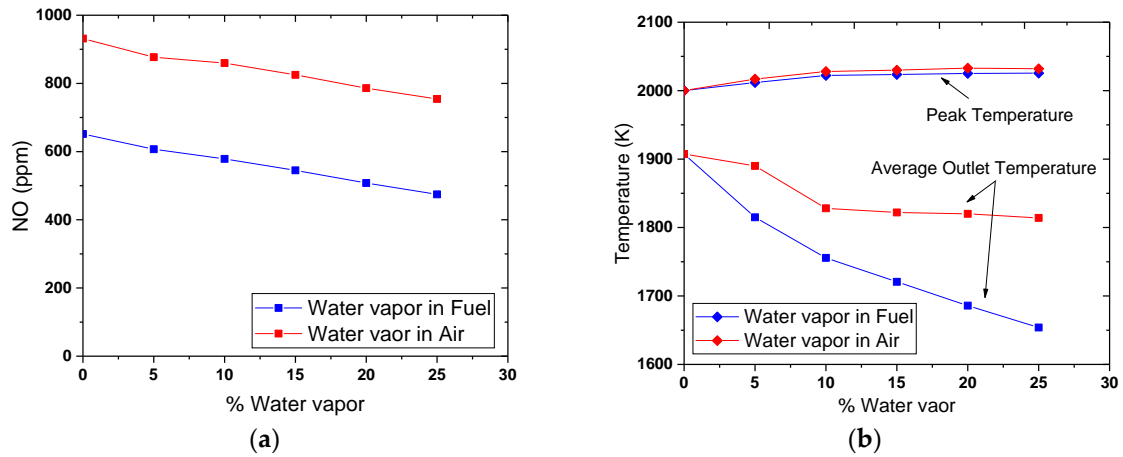


Figure 16. a) NO produced, b) distribution peak, and average outlet temperature.

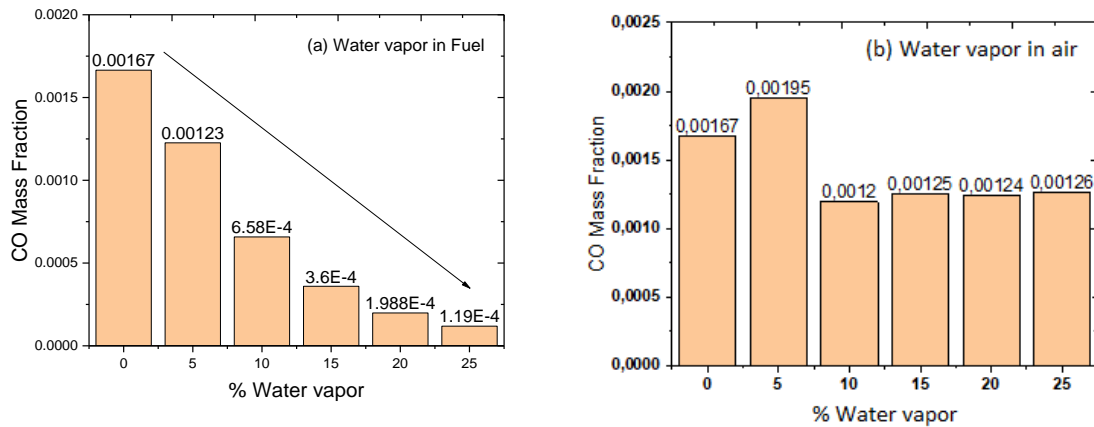


Figure 17. Mass fraction of CO (a) for vaporized water in fuel; (b) for vaporized water in air

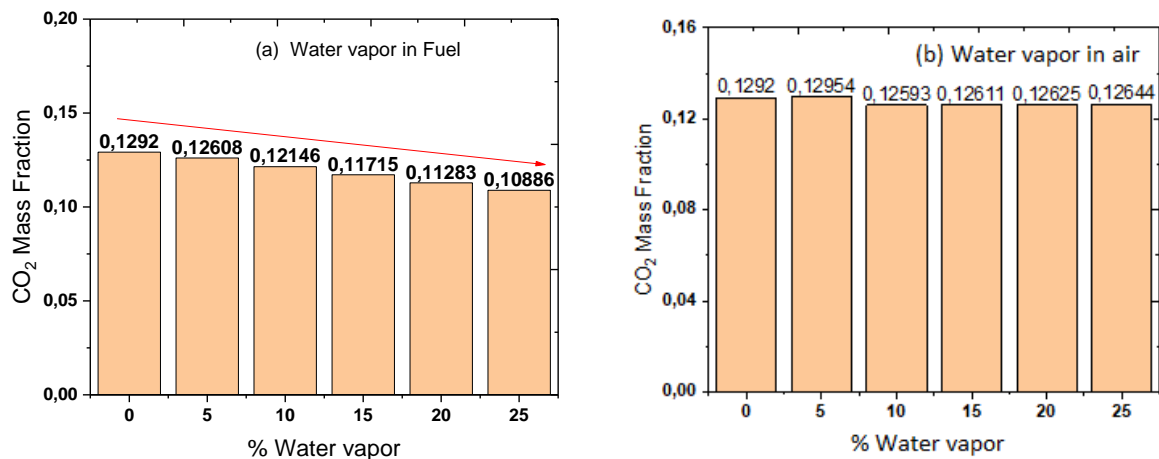


Figure 18. Mass fraction of CO₂: a) for vaporized water in fuel, b) for vaporized water in air

The behavior of the evolution of the CO mass fraction is illustrated in figure 17 for the two simulation cases. It is noted that a value of 14 times less CO than the flame containing no water vapor, i.e., 0% water vapor in the methane. Figure 18 a clearly shows the effect of adding water vapor to methane on the distribution of the CO₂ mass fraction. As the amount of injected water vapor increases from 0% to 25%, the CO₂ concentration drops from 0.1295 to 0.1088. Consequently, dilution of the air by water vapor results in a nearly constant variation

(figure 18 b). There is a clear difference between 0.1292 and 0.1294 indicating that there is no correlation between the percentage of water vapor added to either natural gas or air.

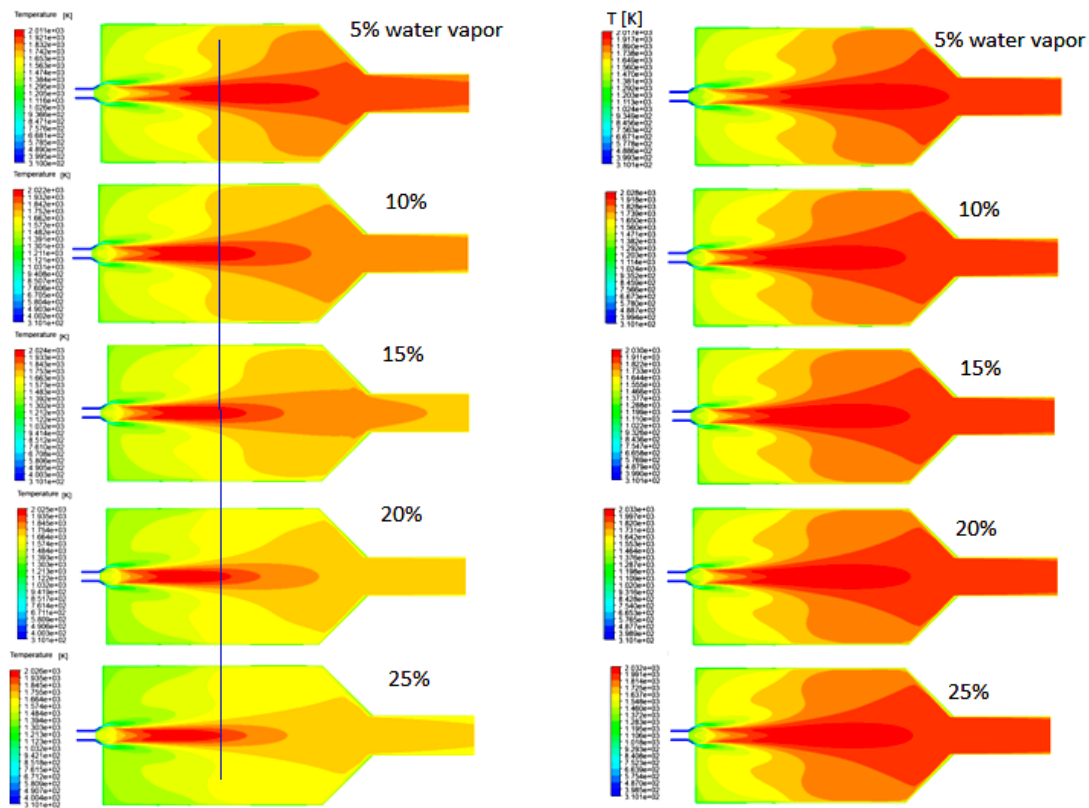


Figure 19. Contours of static temperature (K): Vapor water added to the fuel. (b) Vapor water is added to the air

4. Conclusion

This study evaluated the application of the Steady Laminar Flamelet Model (SLFM) coupled with the detailed GRI-Mech 3.0 mechanism for modeling non-premixed turbulent combustion in a swirl-stabilized natural gas burner. The simulation results show a perfect correlation with experimental data, especially for the radial evolution of axial and tangential velocities along the combustion chamber axis, and the same for the mass fractions of chemical species such as NO and carbon dioxide. However, there is some difference between the results of the simulations and the experimental measurements in the area of strong gradient i.e. in the recirculation zone, where we note that the evolution of carbon dioxide gives curves quite concordant with this experimental data, these differences may be linked to the turbulence model itself i.e. the anisotropy of the turbulence and to the effects of molecular diffusion. Based on these results, it became clear to us that adding water vapor to natural gas has a significant impact on the combustion system and the toxic substances produced. Diluting the natural gas in our case, purely methane has a remarkable effect on reducing nitrogen oxides (NO_x) because the flame temperature at the center of the combustion chamber has decreased. Dilution of the air by adding water droplets to the spray resulted in a very high flame temperature and, simultaneously, a reduction in NO pollutant emissions. In conclusion, this work demonstrates that the SLFM combustion model is well-suited and effective for studying reactive turbulent flows such as flame diffusion, coupled with a detailed kinetic chemistry model like GRI 3.0. This study contributes to the strategy for removing polluting chemical species from combustion chambers in gas turbines, and this technique appears to be a promising method. Future studies should focus on improving the modeling by using second-order turbulence models such as RSM.

Acknowledgment

This numerical simulation study was conducted in the Mechanical Manufacturing Technology Research Laboratory

Authors' Declaration

The authors declare no conflicts of interest in relation to the publication of this article.

Authors' Contribution Statement

Guessab Ahmed: author of the idea, discussion of results, and writing the text of the manuscript. Bounouar Mokhtari: Carrying out simulations and preparing materials for the handwritten document. Mokhtari Mohamed: Methodology and research concept;

References

1. M.M. Nelissen, Diss: Modelling Differential Diffusion in Turbulent Non-Premixed Hydrogen Flames, Delft University of Technology, The Netherlands (2021).
2. ANSYS Fluent, Theory guide, CFD Experts Simulate the Future, 2024.
3. N. Peters, Progress in Energy and Combustion Science **10**(3) (1984) 319.
4. X. Wen, A. Shamooni, O.T. Stein, K. Tainaka, D. Meller, A. Kronenburg, A.M. Kempf, and C. Hasse, Proc. Combust. Inst. **40**(1-4) (2024) 105470.
5. G. Boyer, U. Chikkabikkodu, J. Aguilera, F. Richard, and A. Mura, J. Phys. Conf. Ser. **2885** (2024) 012053.
6. B. Kruljevic, N.A.K. Doan, P. Breda, M. Pfitzner, and I. Langelles, Physics of Fluids **35**(5) (2023) 055114.
7. M.M. Nejaamtheen and J.Y. Choi, Energies **18**(1) (2025) 1.
8. M. Mayrhofer, M. Koller, S. Peter, P. Rene, and H. Christoph, Applied Thermal Engineering **183**(1) (2021) 116190.
9. A. Li, Y. Liu and X. Zhang, Journal of Aerospace Power **38** (2023) 1083.
10. H. C. Noume, V. Bomba, M. Obounou, H. E. Fouda and F. E. Sapnken, Journal of Energy Resources Technology, Transactions of the ASME **143**(11) (2021) 112303.
11. A.A.V. Perpignan, A.G. Rao, and D.J.E.M. Roekaerts, Progress in Energy and Combustion Science **69** (2018) 28.
12. M. Bounouar and A. Guessab, WSEAS Transactions on Fluid Mechanics **18** (2023) 272.
13. D.A. Lysenko, I.S. Ertesvag, and K.E. Rian, Flow Turbulence and Combustion **93**(4) (2020) 577.
14. Z. Wei, M. Li, S. Li, R. Wang, and C. Wang, ACS Omega **6**(37) (2021) 23643.
15. A. Ortolani, J. Yeadon, B. Ruane, C. Paul, and M.S. Campobasso, Results in Engineering **23** (2024) 102392.
16. S. Valencia, C. Celis, and L.F.F. da Silva, Journal of the Brazilian Society of Mechanical Sciences and Engineering **43** (2024).
17. IEN, CFD simulation of syngas/natural gas co-combustion, European Union report No. 723803 (2018).
18. M. Moataz, E.E. Khalil, H. Haridy, and M.A. Yehia, Journal of Power and Energy **273** (2023) 198.
19. V. Rajabi and E. Amani, Heat Transfer Engineering **40**(3-4) (2018) 346.
20. H. Gómez, M. Calleja, and L. Fernández, Energy **185** (2019) 15.
21. S.S. Romero, Diss.: Gas radiation model applicable to CFD simulations in combustion processes, Higher Technical School of Industrial Engineering, Madrid, Spain (2016).
22. C.V. Tommaso, V. Ceglie, F. Fornarelli, M. Torresi, and S.M. Camporeale, Proc. 75th National ATI Congress, Rome (2020).
23. Y. Sujeet and S.S. Mondal, Proc. 45th National Conference on Fluid Mechanics and Fluid Power (FMFP), Bombay (2018).
24. H. Di, Y. Yusong, K. Yucheng, and W. Chaojun, Applied Sciences **11**(9) (2021) 9410.

25. I. Fernandez and J. Manuel, Diss: Study of combustion using a computational fluid dynamics software (ANSYS), Universitat de Barcelona, Barcelona (2015) 71p.
26. A. Sayre, N. Lallement, J. Dugué, and R. Weber, Scaling characteristics of aerodynamics and low-NOx properties of industrial natural gas burners: The SCALING 400 study, Part IV: The 300 kW BERL, International Flame Research Foundation (2000) 136p.
27. T.H. Shih, W.W. Liou, A. Shabbir, Z. Yang, and J. Zhu, *Computers & Fluids* **24**(3) (1995) 227.
28. GRI-Mech 3.0, The Gas Research Institute, <http://combustion.berkeley.edu/gri-mech/> (Accessed 12.08.2024).
29. Gambit 2.2, Tutorial Guide, September (2004) 630p.